communications earth & environment

ARTICLE

https://doi.org/10.1038/s43247-022-00658-5 OPEN

Authigenic clays as precursors to carbonate precipitation in saline lakes of Salar de Llamara, Northern Chile

Erica P. Suosaari[1,2,3✉], Ioan Lascu[1], Amanda M. Oehlert[2], Paola Parlanti[4,5], Enrico Mugnaioli[6], Mauro Gemmi[5], Paul F. Machabee[1,7], Alan M. Piggot[3], Alvaro T. Palma[8] & R. Pamela Reid[2]

The Salar de Llamara, Atacama Desert is host to saline lakes known as Puquios, which are possible analogs for lakes on early Earth or Mars. Here we examine associations between microbial communities, Mg-clay minerals, and carbonates in microbial mat samples from the Puquios using scanning electron microscopy, energy dispersive X-ray spectroscopy, focused ion beam nanotomography, and transmission electron microscopy. We observe micrometer-scale aggregates of nanocrystalline Mg-clay around cyanobacterial cell sheaths and throughout alveolar networks of microbial extracellular polymeric substances. High-Mn calcite occupies pore spaces and surfaces within the clay matrix. We propose a sequence whereby extracellular polymeric substance networks serve as surfaces for precipitation of Mg-clay, which permineralizes the original microorganisms. Formation of the clay reduces kinetic barriers and provides a suitable substrate for the formation of carbonate minerals. We therefore suggest that authigenic clays are important in the preservation of microbial communities and the precipitation of carbonates in non-marine settings such as the saline lakes of the Atacama Desert.

[1] Department of Mineral Sciences, National Museum of Natural History, Smithsonian Institution, Washington, DC 20560, USA. [2] Rosenstiel School of Marine and Atmospheric Science, University of Miami, Miami, FL 33149, USA. [3] Bahamas Marine EcoCentre, Miami, FL 33158, USA. [4] Nanofabrication and Imaging Center, George Washington University, Washington, DC 20052, USA. [5] Istituto Italiano di Tecnologia, Center for Materials Interfaces, Electron Crystallography, 56025 Pontedera, (PI), Italy. [6] Department of Earth Sciences, University of Pisa, Via S. Maria 53, 56126 Pisa, Italy. [7] Skidmore College, Saratoga Springs, New York, NY 12866, USA. [8] FisioAqua, Las Condes, 7550024 Santiago, Chile. ✉email: erica.suosaari@gmail.com

An association between Mg-clay and carbonate minerals has increasingly been recognized across a wide range of depositional environments in both modern and ancient settings in association with microbialites (Supplemental Table S1). In modern environments, close associations of Mg-clay with microbes and exopolymeric substances (EPS) suggest that precipitation of this clay may be microbially-influenced. Indeed, it has been proposed that authigenic Mg-clay and subsequent carbonate deposition in microbialites enhance the structural integrity of microbial buildups and, as such, Mg-clays may be a vital component of microbialite growth in non-marine environments[1], and may even be responsible for the preservation of fine-scale microbial features within microbialite microfabrics[2]. In addition, precipitation of carbonate minerals like aragonite was suggested to occur as a result of degradation of cyanobacterial organic matter by heterotrophic bacteria, often juxtaposed with Mg-clay[3,4]. Despite the recognition of the common co-occurrence of Mg-clay and carbonate in modern microbial sedimentary environments, the role of clay formation in the facilitation of carbonate mineral precipitation remains unknown.

In this paper, we investigate a modern terrestrial saline lake and peripheral pond system in the Salar de Llamara, a lacustrine depositional environment located in the Atacama Desert of northern Chile, where Mg-clays and carbonates co-exist as microbial sediments. Using focused ion beam scanning electron microscopy (FIB-SEM) to show the relationship between microbes, organic matrices, and minerals in a high-resolution spatial framework, we were able to elucidate the process of mineral precipitation dynamics at the nanoscale, and also identify the potentially important role that authigenic clays play in the preservation of evidence of microbial communities. Previously, FIB-SEM was used on samples from Mexican crater lakes to highlight cavities preserved within Mg-clay where former microbial cell sheaths existed, suggesting that authigenic clay may offer enhanced preservation potential of microbial communities[2]. In this paper, we use FIB-SEM to examine how the microbes and associated EPS provide surfaces for Mg-clay formation, which in turn sets the stage for the precipitation of carbonate on the clay and within void spaces. In particular, we address the question of whether Mg-clays are important precursors for microbial carbonate precipitation in this and similar lacustrine settings. If so, clay-carbonate mineral associations may assist identification of microbially-produced carbonate in the rock record and aid in paleoenvironment interpretation.

Study site: the Puquios, Salar de Llamara, Atacama Desert. The Puquios of the Salar de Llamara are located in the Tarapacá Region of the Atacama Desert in Northern Chile between 18° and 22° S (Fig. 1). Positioned atop the evaporites of the Soledad Formation[5–9], the Puquios were created by the dissolution of subsurface evaporites by local phreatic water[10,11]. The Puquios are composed of four saline lakes and a series of smaller ponds, the majority of which are located between Puquio 1 and 2 in an area termed the "Transition Zone"[12–14], which is the focus of the present study. The ponds within the Transition Zone are hydrologically connected, with ground water flow from southwest to northeast, and increasing electrical conductivity from Puquio 1 to Puquio 2[7,12,14]. The observed environmental gradients are the result of evaporation and local sub-surface water-rock interactions, which impact brine composition *sensu*[7,15,16]. These physical, chemical, and microbial feedbacks across the Puquios system are described in detail by Oehlert et al.[14]. This heterogeneity drives variations in benthic microbial mat morphologies that are present throughout the Transition Zone where microbial mats host Ca-Mn carbonate minerals, in close association with Mg-clay[12,13]. As such, the Transition Zone was an ideal locale to collect samples to examine the various stages of the clay-carbonate association.

Results

In situ environmental parameters. In situ parameters measured at the time of sample collection are reported in Table 1. Bottom water measured in P163 (orange/brown bulbous mat) was characterized by higher pH and DO, was less reducing, and lower EC, salinity, and turbidity than bottom water measured in P31 (orange gel mat). Temperature was not reported as pond water temperature varies greatly over the course of the day.

Microbial mat characterization. Optical microscopy was employed to observe the relationship between cells/organic materials and minerals. Microscopic examination of the orange/brown bulbous mat sample collected from pond P163 shows filamentous cyanobacteria as a common component in both plane- and cross-polarized light (Fig. 2a–c). Viewed in thin section, the cross-sections of filaments appeared hollow, with cell margins having first-order birefringence colors with sweeping extinction, reflecting a large number of small crystals precipitating along the surface of the cell sheaths (Fig. 2b, c). When the sample was stained with crystal-violet and reexamined under plane-polarized light, the stain highlighted an abundance of bacterial filaments and EPS networks (Fig. 2d–f). Abundant diatoms also were present.

Conventional SEM analyses were completed to observe the fine-scale relationship between microbes and minerals. Investigation of sample P163 and sample P31 revealed an intimate association of microbes and minerals at various stages of mineralization (Fig. 3). From pond P163 (Fig. 3a), in the orange/brown bulbous mat sample (Fig. 3b), Mg-clay was observed forming initially around the cell sheaths as thin, micrometer-scale precipitates (Fig. 3c–e). This precipitation of Mg-clay along the cell sheath appears to increase in thickness with time resulting in coatings that ranged up to several tens of micrometers in diameter (Fig. 4d–f). Mg-clay also was observed throughout the EPS alveolar networks, as shown in the orange gel mat sample collected from pond P31 (Fig. 3f–j). Pockets of carbonate were observed within and around the clay (Fig. 3h, i, k). In the P31 sample, the EDS of Mg-clay surrounding microbial filaments and enveloping EPS networks surrounding the cells contained minor amounts of manganese incorporated into the matrix (Fig. 3j). EDS of the carbonate material revealed strong peaks for both calcium and manganese (Fig. 3j, k).

FIB-SEM nanotomography was completed to show nanoscale microbe-mineral-precipitation dynamics through cross-sectional volume reconstruction of sampled areas. For the sample of the microbial mat classified as orange/brown bulbous mat collected from pond P163, this reconstruction indicates the 3-dimensional framework of the micrometer-scale Mg-clay precipitates around the cell, which consists of nanocrystals forming a band along the cell sheath. At the cell exterior, the Mg-clay accumulated as spaced-out rosettes of nanocrystals within 5–10 µm of the cell wall. More sparse, individual Mg-clay nanocrystals occur at the interior of the cell, within 1–2 µm of the cell wall (Fig. 4a–c, Fig. 5, Supplementary Video 1). FIB-SEM nanotomography of P31a targeted a longitudinal section of a filamentous cell at a later stage of Mg-clay formation, with a dense aggregation of nanocrystals around the cell sheath, up to 20 µm in thickness. Rosettes of Mg-clay nanocrystals occur in the cell interior, within 3–5 µm of the cell wall (4d–f). The FIB-SEM nanotomography of P31b shows precipitates of Mg-clay together with Ca–Mn carbonate. Here, the

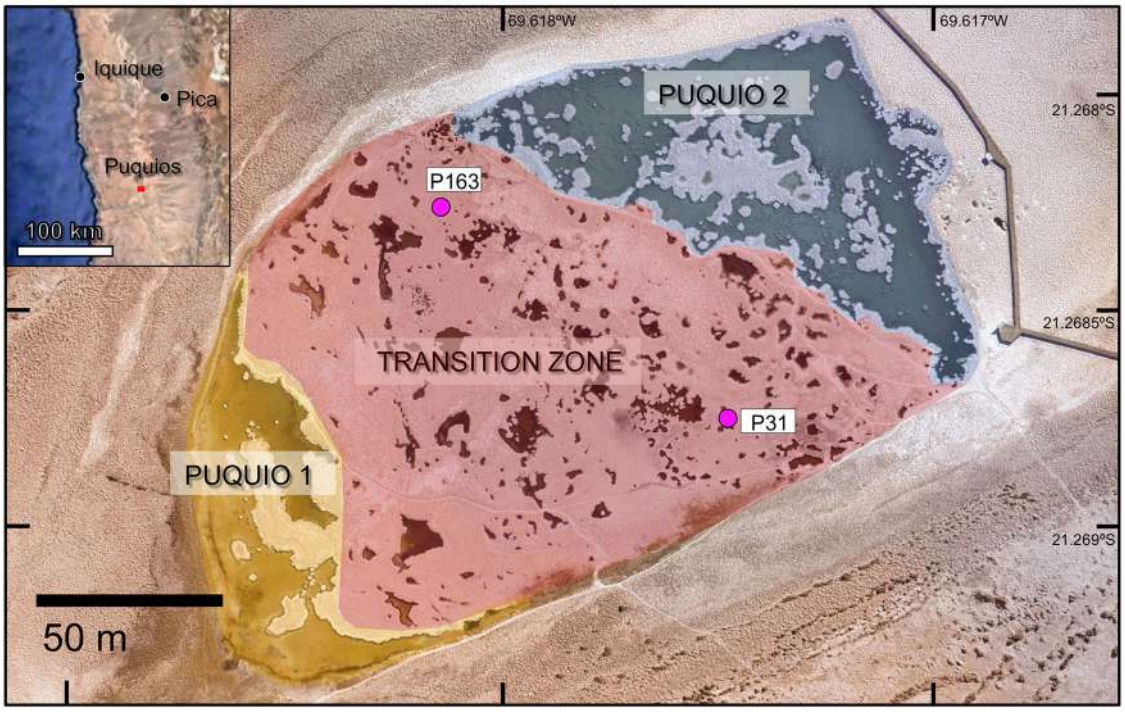

Fig. 1 Study site. Location map of the Puquio 1 – Puquio 2 system of the Salar de Llamara showing Puquio 1 highlighted in yellow, the Transition Zone highlighted in red, and Puquio 2 highlighted in blue. Collected samples are shown with pink markers and labelled by pond number. Inset with geographic context: Google, Landsat/Copernicus, SIO, NOAA, U.S. Navy, GEBCO, LDEO-Columbia, NSF, NOAA. Base map: drone imagery collected in November 2017.

Table 1 Sample locations, descriptions, and in situ water parameter measurements.

	Sample	
Sample ID	PQ-171130-P1-05	20190321-P31
Location	P163	P31
Longitude (dd)	−69.61816602	−69.617478
Latitude (dd)	−21.26828704	−21.2687605
Date	11/30/17	3/21/19
Description	orange/brown bulbous mat	orange gel mat
pH	8.36	7.4
ORP (mV)	−6.8	−228
EC (µS/cm)	47760	114400
Salinity (psu)	24.94	59.67
DO (mg/L)	7.42	1.39
Turbidity (FNU)	0.3	121.1

Mg-clay appears to precipitate and accumulate along EPS alveolar networks, whereas the carbonate precipitates within and around the Mg-clay matrix and fills void spaces (Fig. 4g–i). Where the Mg-clay is porous, the clay and carbonate are interfingered, whereas where the Mg-clay is dense, there is a distinct boundary between the clay and carbonate minerals (Fig. 6, Supplementary Video 2).

TEM analyses (Fig. 7) revealed the Mg-Si (Fig. 3a) was amorphous to nanocrystalline, with diffraction rings showing interplanar distances of 4.6, 2.7, 1.5, 1.3 and 1.2 Å (Fig. 7b). These distances correspond well to expected *hk0* diffraction lines of lizardite, but may be also consistent with other more complex phyllosilicates like Mg-rich smectites. By comparison, the Ca-Mn carbonate was nanocrystalline, composed of relatively well-developed crystals, with average sizes <100 nm and maximum sizes of about 300 nm. For these crystals, EDS spectroscopy reveals a Ca:Mn elemental ratio of about 1:1 (Supplemental Table S3). 3DED reconstructions showed a rhombohedral cell, with parameters $a = 4.9(1)$ Å and $c = 16.4(3)$ and reflection extinctions pointing to space group $R\text{-}3c$ (Fig. 7c, d). Composition and cell parameters would be consistent with the mineral kutnohorite $(Ca,Mn)(CO_3)_2$, but the occurrence of clear extinctions along c^* suggests a high-degree of disorder in the Ca-Mn occupancy, and not orderly alternated as would be expected in kutnohorite. Therefore, the mineral could also be called high-Mn calcite.

Discussion

Results above document primary precipitation high-Mn calcite forming within benthic microbial communities in close association with microbes and extracellular polymeric substance (EPS), which may have influenced mineral formation.

Role of Mg-clay in carbonate precipitation. The analysis of samples collected across the Transition Zone in the Puquios using SEM, FIB-SEM nanotomography, combined with in situ physicochemical measurements, provides insight into the role of Mg-clay in carbonate precipitation within microbial mats. Carbonate minerals in the Puquios occur together with Mg-clays, and the close association of both Mg-clay and carbonate minerals with microbes and EPS support the biological influence on mineral precipitation. These findings from the Salar de Llamara evaporitic environment, coupled with the increasingly recognized co-occurrence of Mg-clay with microbial carbonates in other environments (Supplemental Table S1), raises the question: is authigenic clay formation a precursor for microbially-influenced carbonate precipitation? In the Puquios, the four-stage model we detail below suggests that the answer is yes.

Stage 1—The microbial community produces EPS that makes up cell sheaths and forms an alveolar network (Fig. 8a). EPS accumulates outside the cells as a hydrated, polyanionic matrix that

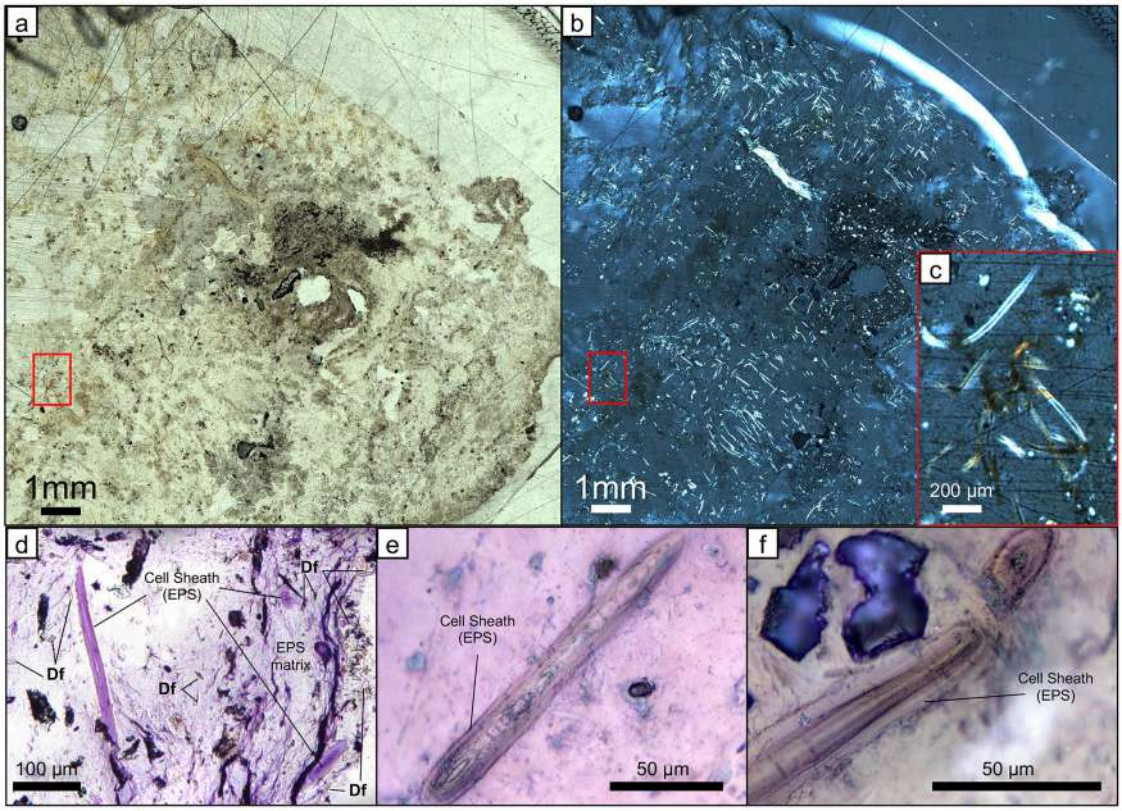

Fig. 2 Optical micrographs showing filamentous cyanobacteria encased in Mg-clay. a Sample in plane-polarized light; filaments difficult to discern, **b** same sample image shown in cross-polarized light; filaments are highlighted by first-order birefringence colors, **c** higher resolution image from red box in (**a**, **b**) showing detail of filamentous cyanobacterial cells (from[12] Fig. 6b), **d**–**f** Thin section stained with crystal-violet and shown in plane-polarized light with the stain highlighting biomass; diatom frustules 'Df' are abundant throughout the sample as shown in (**d**).

provides both physical and chemical protection, and helps to buffer cells from physical stressors such as UV radiation, desiccation, changes in salinity and temperature, etc.[17]. EPS occurred in all collected microbial mat samples, particularly observable when stained with crystal violet, and occurred as a well-defined, porous and tangled network in thin section (Fig. 2d).

Stage 2—Biologically-influenced nanocrystalline Mg-clay forms in and along the cell sheaths, as well as on the surrounding EPS network (Fig. 8b). Sub-micrometer rosettes of Mg-clay nanocrystals form along cell sheaths (Fig. 2c, Fig. 3c, e, Fig. 4a–f, Fig. 5) and on EPS surfaces throughout alveolar networks (Fig. 3c, d, Fig. 4g–i. Figure 6). Around cell sheaths, these rosettes form dense accumulations directly around the sheath where they use the sheath as a surface to accumulate, replicating the morphology of the sheath and becoming more dispersed with increasing distance from the cell sheath on both the interior and exterior of the cell (Fig. 4b, c, Fig. 5). Precipitation of authigenic Mg-clay on microbial sheaths composed of EPS and surrounding EPS networks requires magnesium (Mg^{2+}) and silica ($SiO_{2\ (aq)}$) sources, and a pH above ~8.2[2,18–20]. First, photosynthetic activity of the microbial community increases the local pH *sensu*[3] in the surrounding microenvironment, which can considerably impact how EPS binds cations[17,21,22], while also controlling the order and location of mineral precipitation[23]. As such, EPS is responsible for altering the brine chemistry in the microenvironment by effectively binding and/or concentrating a range of metal cations[17,24]. Electron microprobe analysis showed that EPS can be generally rich in Ca^{2+} and depleted in cations like P^{+} and Mg^{2+} [24]. In some environments, EPS has been shown to bind up to 8 times more Ca^{2+} ions than Mg^{2+} ions[25]. This removal of Ca^{2+} ions from the surrounding microenvironment would inhibit the initial precipitation of $CaCO_3$[25–31], while enriching the microenvironment in Mg^{2+} *sensu*[2]. Additionally, elevated pH increases the solubility of silica[23]. Diatom frustules were abundant throughout the transition zone in the Puquios and observed in collected samples at different states of dissolution (Fig. 3c), as a result of the elevated pH *sensu*[18,32,33]. The dissolution of diatom frustules increases the local activity of silicic acid, which, paired with high activities of Mg^{2+}, favors Mg-clay precipitation[2]. Mg-clays accumulate directly onto the EPS surfaces, which act as optimal nucleation sites[21]. This biologically-influenced mineral precipitation may commence while the cell is still living, however as Mg-clay also forms in the cell interior (Figs. 3d, 4d–f, 5, and Supplementary Video 1), the Mg-clay precipitation may begin and/or continue post-mortem.

Stage 3—Mg-clay develops into thicker accumulations and EPS is degraded releasing Ca^{2+} ions (Fig. 8c). Once the Mg-clay mineral has covered the original surface (cell sheaths and/or EPS), the newly formed reactive surface is used for continued growth, leading to the dense accumulation of Mg-clay, growing outward from the cell forming a thick covering, often tens of micrometers in size (Fig. 4d–f), and also filling void spaces throughout the EPS matrix. EPS polymers in the biomass are later broken down by heterotrophic degradation, which liberates Ca^{2+} cations complexed within EPS into the surrounding microenvironment[26,28,34–36]. These processes set the stage for carbonate precipitation.

Stage 4—Carbonate precipitates within and around the Mg-clay matrix and fill void spaces (Fig. 8d). Where Mg-clay forms on the EPS alveolar networks and abundant pore spaces exist, high-Mn

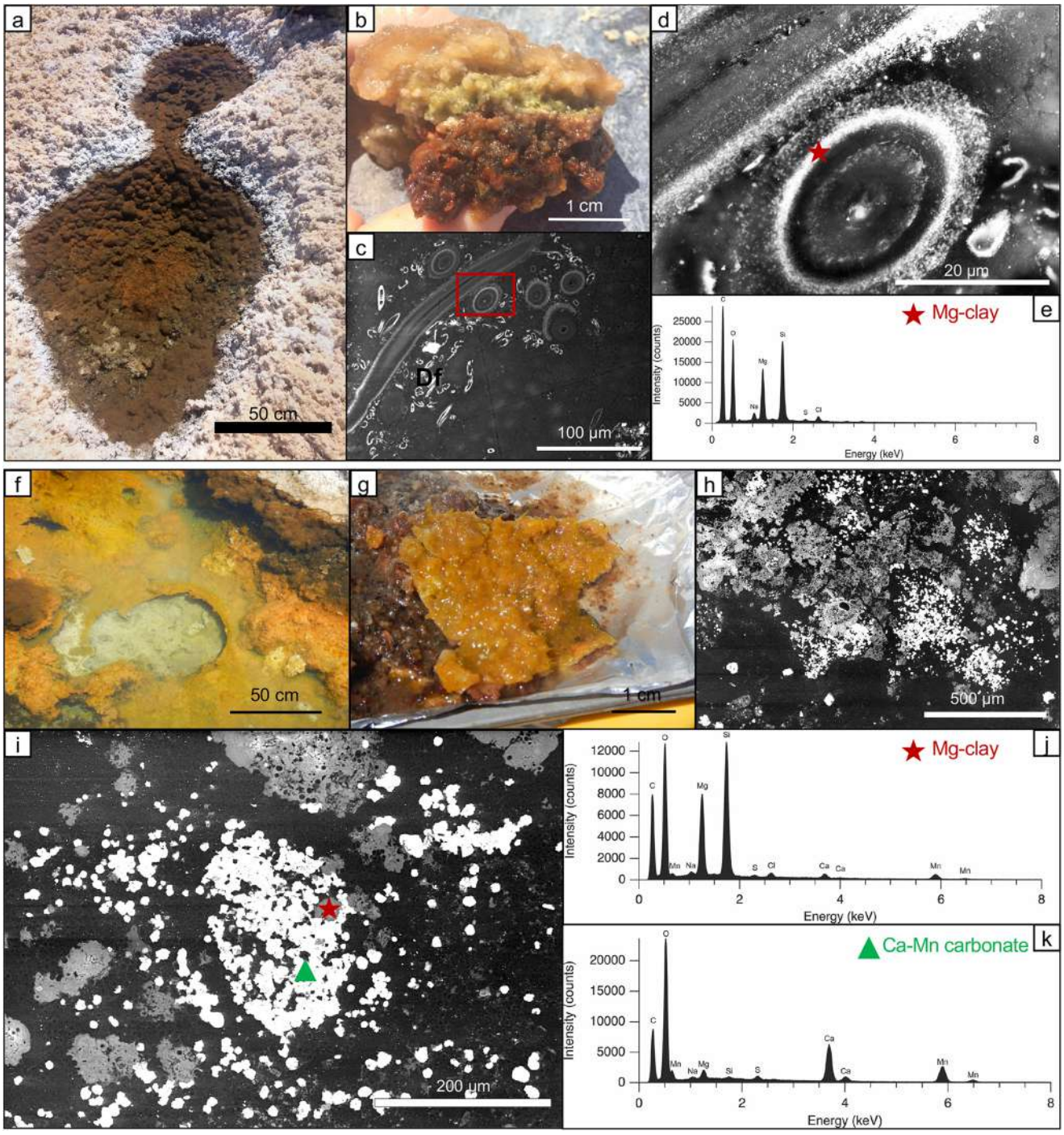

Fig. 3 SEM and EDS of samples. a–e Orange/brown bulbous mat (sample P163): **a** Depositional setting in pond, **b** hand sample (*from*[12] Fig. 6a), **c** SEM image of filamentous cyanobacteria surrounded by Mg-clay, **d** higher resolution SEM image from red box in (**c**) showing Mg-clay precipitation around the cell-sheath; diatom frustules 'Df' are abundant (**e**) EDS spectrum from spot indicated by red asterisk in (**d**). Orange gel mat (P31): **f** Depositional setting in pond, **g** hand sample, **h**, **i** Mg-clay (gray) throughout an EPS alveolar network together with intermixed accumulations of Ca–Mn carbonate (white), **j**, **k** EDS spectra from spots indicated in (**i**). See Supplemental Table S3 for all eZAF smart quant results.

calcite was closely juxtaposed within the Mg-clay matrix, with Mn^{2+} incorporated into the carbonate likely as a result of elevated Mn^{2+} concentrations in the pond water. Where the Mg-clay accumulations are dense and without pore spaces, high-Mn calcite was observed forming along clay margins (Fig. 6). Mg^{2+} can inhibit $CaCO_3$ precipitation[37,38], and in the lab, it has been shown that smectite enhances the nucleation of calcite in Mg-free environments[39]. The precipitation of calcite proceeds after the Mg^{2+} ions remain complexed in the Mg-clay, and the microenvironment experiences an increase in local carbonate and calcium activities through the degradation of organic matter creating a zone of supersaturation within the microbial mat, which drives mineral precipitation[21,25,26,40–42]. Mg-clay is an ideal substrate for the nucleation of carbonate *sensu*[20], which begins to fill voids within and around the clay surface (Fig. 4g–i, Fig. 6, Supplementary Video 2).

The 4-stage model summarized above, based on our high-resolution reconstructions from FIB-SEM, shows the spatial

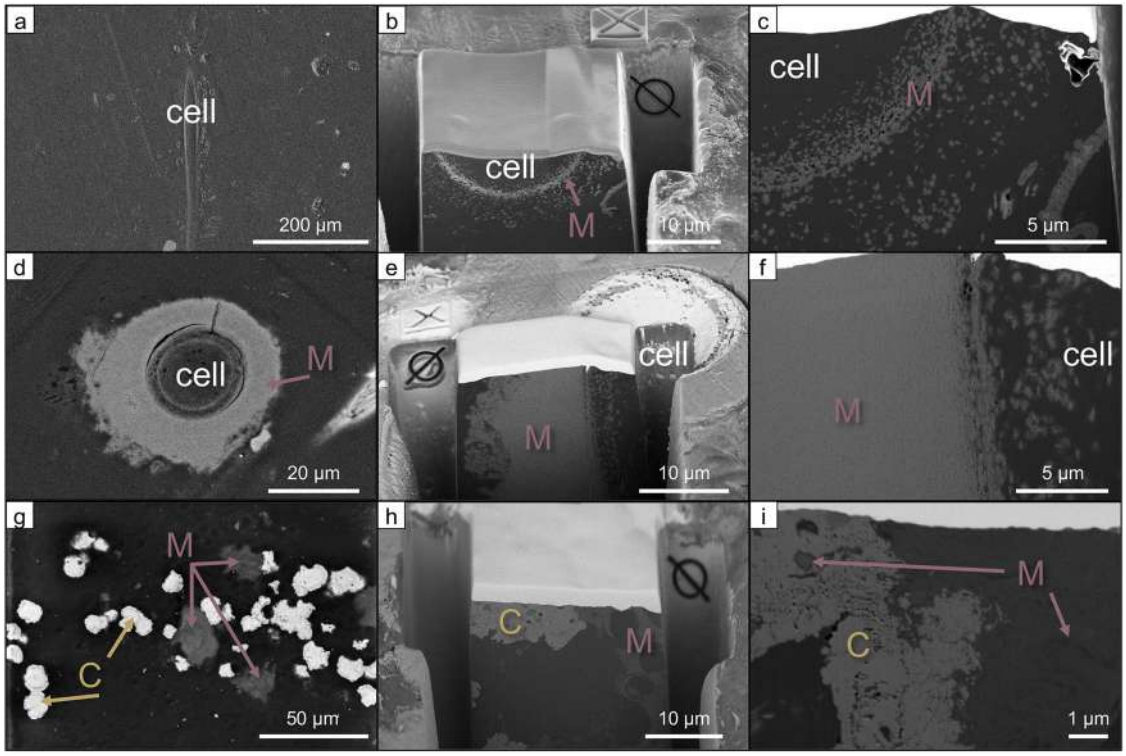

Fig. 4 FIB-SEM nanotomography. Mg-clay (M), Ca–Mn carbonate (C). **a**–**c** Orange/brown bulbous mat sample collected from pond P163: **a** longitudinal section of filamentous cyanobacterium with Mg-clay surrounding the cell sheath, **b** FIB milling area showing the cross section of the cell sheath surrounded by Mg-clay, **c** Mg-clay nanocrystals form a band around the cell sheath, with a more spaced-out arrangement of rosettes accumulating around the exterior of the cell, and sparse individual nanocrystals at the interior of the cell. Orange gel mat sample collected from Pond P31: **d** cross section of a filamentous cyanobacterium cell with a thick, dense accumulation of Mg-clay surrounding the cell sheath, **e** FIB milling area, parallel to the cell sheath, **f** dense Mg-clay aggregation around the cell sheath with nanocrystals rosettes towards the interior of the cell, **g** Mg-clay throughout an EPS alveolar network in association with Ca–Mn carbonate, **h** FIB milling area of the carbonate-clay boundary, **i** detail of the boundary showing interfingering of Mg-clay and carbonate in the upper left.

relationships between Mg-clay and carbonate and illustrates mineral precipitation dynamics at the nanoscale. The model further sheds light on the potential importance of Mg-clay in microbial carbonate precipitation pathways. Carbonate mineral deposition in the Puquios Transition Zone appears to result from a culmination of the metabolic activities of microbial communities, cation binding properties of the biomass, and organic matter decay. Our results suggest that the precipitation of Mg-clays on EPS surfaces is a critical step in the formation of microbial carbonate, whereby the clays, due to their high reactivity, modify brine chemistry in their immediate microenvironment, and help overcome kinetic barriers *sensu*[43,44].

Comparison with other environments. Microbially-influenced precipitation of carbonate minerals in conjunction with Mg-clays has been documented in association with microbialites in a number of lacustrine environments. Recent studies have shown Mg-clays in association with microbialites in lake systems along the Western Australian coastline including The Yalgorup Lakes, south of Mandurah[1,45] and Lake Thetis, north of Perth;[4] in Mexican crater lakes[2]; around the shores of Mono Lake[46]; and in Great Salt Lake[3] (See Supplemental Table S1 for a more comprehensive list). In all of these studies, the Mg-clays are formed in microbial mats associated with microbes and EPS. Some authors have argued that authigenic clay and subsequent carbonate deposition in microbialites may enhance preservation of fine-scale microbial features within the microfabrics[2]. In contrast, others have argued that the clay-carbonate precipitation pathway may destroy evidence of microbes within microfabrics, making microbial origin difficult to discern in the fossil record[1].

Although the components forming microbialites often are the same, the processes of formation may differ For example, in Lake Satonda, micrometer-sized microbialite subfossils contain alternating layers of amorphous Mg-clay and fibrous aragonite[47]. In this lake, cycles of aragonite growth occur on a Mg-calcite impregnated biofilm and once entombed, Mg-calcite was interpreted to have dissolved as a result of heterotrophic decay, liberating Mg^{2+}, which coupled with aqueous silica derived from dissolved diatoms and sponge spicules formed the clay layer. In Mono Lake, Souza-Egipsy et al.[46] examined the role of Mg-clay in the fossilization of sand tufa endolithic microbial communities, predicting that cell walls adsorb Mg^{2+}, promoting Mg-clay formation post-mortem. Then, after cytoplasmic decay, the cell area becomes infilled with carbonate that displaces the clay matrix[46]. In both of these environments, carbonate and Mg-clay are intermixed and dependent on one another in the process of mineral precipitation.

Microbialites examined in Lake Clifton[1,45] and in Great Salt Lake[3] shared the most similar pathway to that observed in the Puquios. In Lake Clifton modern microbialites, Burne et al.[1] described the Mg-clay stevensite as first forming around the cyanobacterial sheaths, and subsequently in the EPS alveolar network, and continuing to accumulate and fill in the alveolar network as EPS degraded. Stevensite was interpreted to form as a result of diatom dissolution in waters of elevated pH, in concert with biologically lowered $CO_3^{2-}$and Ca^{2+} activities[1]. After the

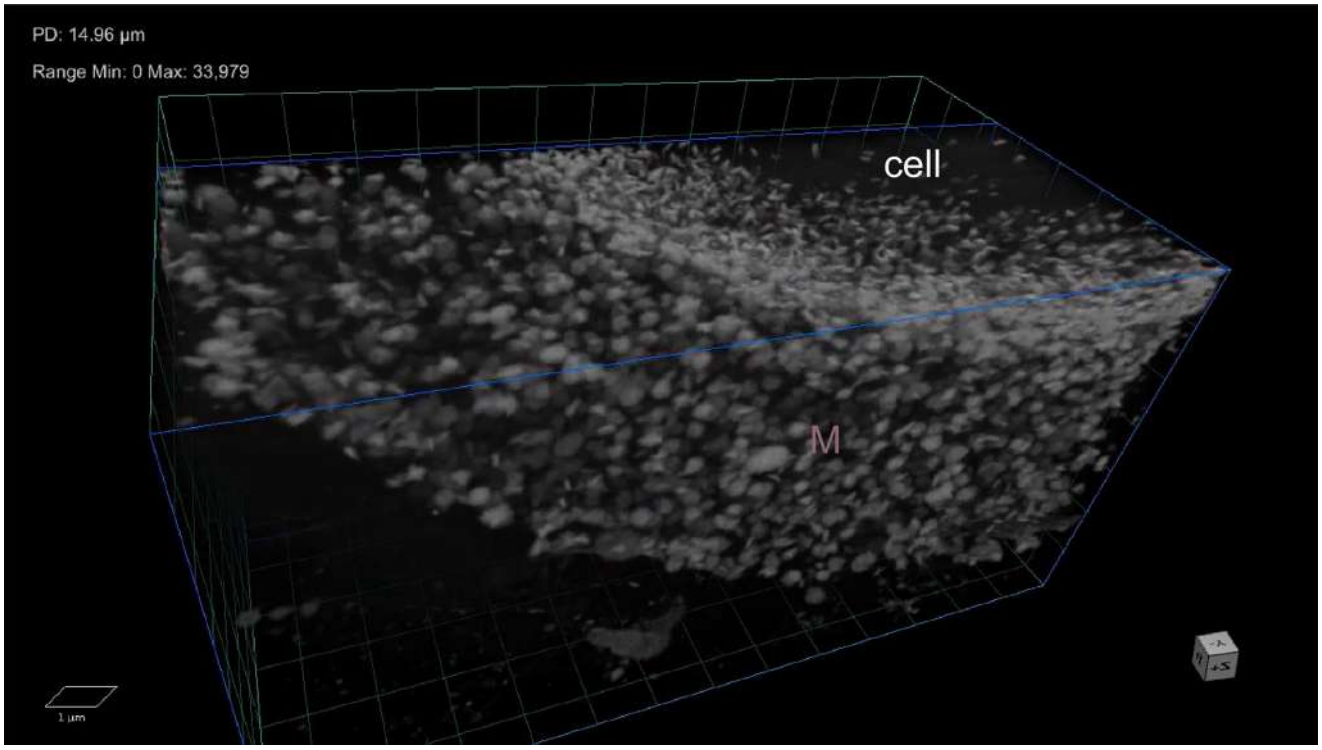

Fig. 5 FIB-SEM nanotomography reconstruction from P163. 3D reconstruction of part of the ROI from P163, showing the spatial relationships between the Mg-clay nanocrystals (M) and the cell, densest around the cell sheath, with more dispersed rosettes at the exterior of the cell and individual crystals at the interior. 3D video reconstruction is available as Supplementary Video SV1.

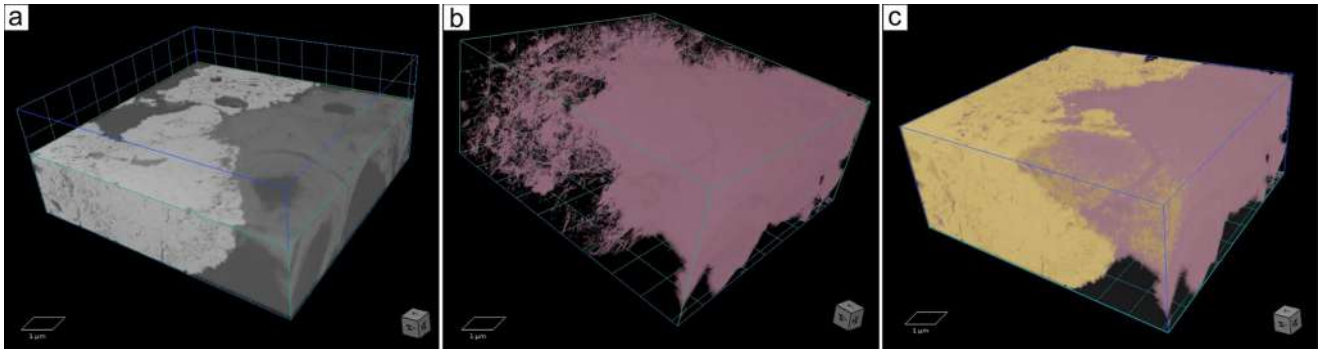

Fig. 6 FIB-SEM nanotomography reconstruction from P31b. 3D reconstruction of part of the ROI from P31b, showing the Mg-clay and Ca-Mn carbonate association: **a** Ca-Mn carbonate (light gray) in juxtaposition with the Mg-clay (mid gray), **b** Mg-clay spatial configuration after removing the carbonate from model, **c** Mg-clay (pink) and Ca-Mn carbonate (yellow) intimately intermingled – block rotated approximately 180 degrees around the vertical axis. 3D video reconstruction is available as Supplementary Video SV2.

microbial material was degraded or entombed, the local $CO_3^{2-}$and Ca^{2+} activities increased enough to induce the formation of abiogenic aragonite, which then overgrew the stevensite fabric[1]. In Great Salt Lake, the microbial and diagenetic steps leading to the mineralization of microbialites[3] were most similar to those leading to formation of microbial carbonate in the Puquios. In Great Salt Lake, Mg-clay accumulates on EPS, followed by aragonite nucleation in the pockets created from EPS and cell degradation[3]. The aragonite precipitation was correlated to hotspots of sulfate reduction where aragonite was observed to replace most of the organic framework[3]. In Great Salt Lake, an additional stage involves the dissolution of the Mg-clay, coupled with partial dissolution of the aragonite, which results in the precipitation of dolomite[3], a process not observed in the Puquios.

Contrasting with the fundamental role of Mg-clay in Lakes Satonda and Clifton, and Great Salt Lake, precipitation of calcium carbonate was not dependent upon the primary precipitation of Mg-clay in the Mexican Crater lakes[2]. Here, patches of calcium carbonate were observed growing within a Mg-clay (kerolite) matrix. Precipitation of the minerals was induced either as a result of the chemical composition of the surrounding lake water, or as a result of microbial influence, with kinetics determining the formation of calcium carbonate or kerolite[2]. This investigation focused mainly on the formation of kerolite in three different lakes, which was precipitated in waters with elevated pH, where dissolved diatoms provided the silica for kerolite precipitation, and microbial cells provided surfaces for kerolite nucleation[2]. FIB-SEM from this study showed that numerous coccoid and filamentous cells were surrounded by kerolite and preserved as empty cavities post cell degradation[2]. Precipitation of carbonate within the kerolite appears strikingly similar to that observed in the Puquios.

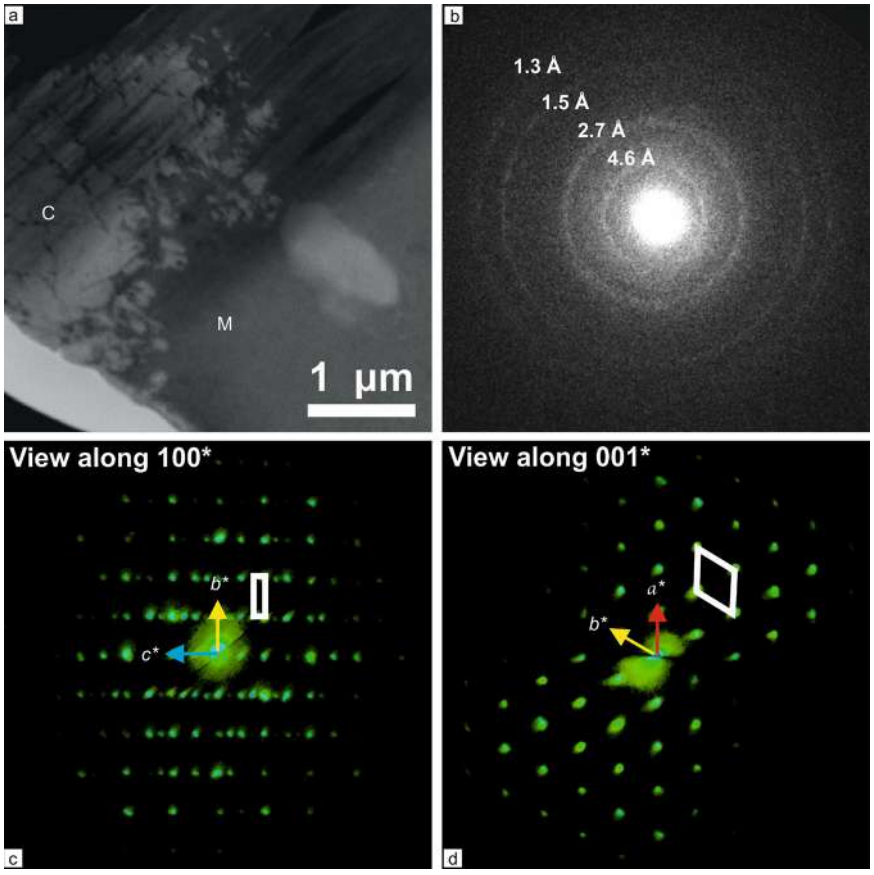

Fig. 7 TEM and electron diffraction analysis of high-Mn calcite–Mg-clay interface. a Image of a FIB lamella showing the typical contact between nanocrystalline high-Mn calcite (labeled 'C' and nanocrystalline-to-amorphous Mg-clay (M). **b** Polycrystalline SAED pattern originating from the Mg-clay. Rings correspond to typical *hk0* interplanar distances of T-O phyllosilicates. **c** Projection along reciprocal axis *a** (100*) and **d** projection of 3D diffraction volume along reciprocal axis c* (001*) of reconstructed 3DED data taken from a single high-Mn calcite crystal of few hundred nanometers in size. Reciprocal cell edges are sketched as quadrilaterals.

Based on our observations in the Puquios, and similarities with Mg-clay carbonate associations in other settings, we suggest that carbonate formation via an authigenic clay precursor is a common precipitation pathway. Moreover, we propose that the formation of biologically influenced authigenic clays is a possible prerequisite for microbial carbonate deposition in some non-marine aqueous environments.

Implications. The extreme environment of the Puquios represents an ideal location for geobiological investigations as this setting is an analog to those that may have existed on early Earth and beyond. Microbial ecosystems, such as those within the Puquios, serve as important hot spots for biosignatures—patterns or products made by the activity of life, rather than by abiotic processes[48–50]. These signatures typically include isotopes that could have been influenced by biological activity, biomarkers like lipids or other chemical compounds produced inside cells, biominerals that are produced directly or indirectly by life, or microfossils such as cellular remains[50]. Because diagenetic processes often can obliterate biosignatures[51], the mineralization pathway proposed here (Fig. 8) and shown at nanometer-scale resolution using FIB-SEM nanotomography (Figs. 4–6, Supplementary Video SV1, Supplementary Video SV2) suggest that microbial biosignatures may include the fine scale mineral association of carbonate and Mg-clay minerals. Although Mg-clay and carbonate associations can form without the direct involvement of microorganisms [39,52 and references therein], we suggest that this fine-scale mineral association also has the potential to act as a biosignature through time.

Alone, the presence of Mg-clay in the rock record is not often attributed to microbial influence unless the deposits are confined to small areas such as microbial mats[20,46,53,54]. Typically, Mg-clays occur in widespread accumulations in alkaline lakes and evaporative basins where the Mg-clay is thought to have precipitated directly from the water column upon supersaturation *sensu*[2,3,55–61]. Mg-clays can also occur in hydrothermal settings where fluids interacted with Mg-rich igneous materials[62], or can be attributed to various weathering profiles dominated by Mg-rich volcanic rocks[63]. They also are interpreted as an early diagenetic phase formed in situ in an alkaline, non-marine environment[59]. Deciphering the environment of formation of Mg-clays throughout the rock record can therefore be an arduous process. Thus, markers and/or mineral associations that may indicate biogenicity have the potential to be important biosignatures.

More research is needed to determine if Mg-clays and proto-clays, like those identified in the Puquios and elsewhere, convert to more stable clay phases through time[64] and become preserved in the rock record[65]. Conversely, authigenic clays may degrade through thermodynamic undersaturation of Mg-clay[20]; thus, the important role Mg-clays play in the formation of microbial carbonate may be largely unrecognized in the geological record. Our findings result in a fundamental shift in our understanding of how microbes influence mineralization pathways, provide insight into the timing and order of events involved in

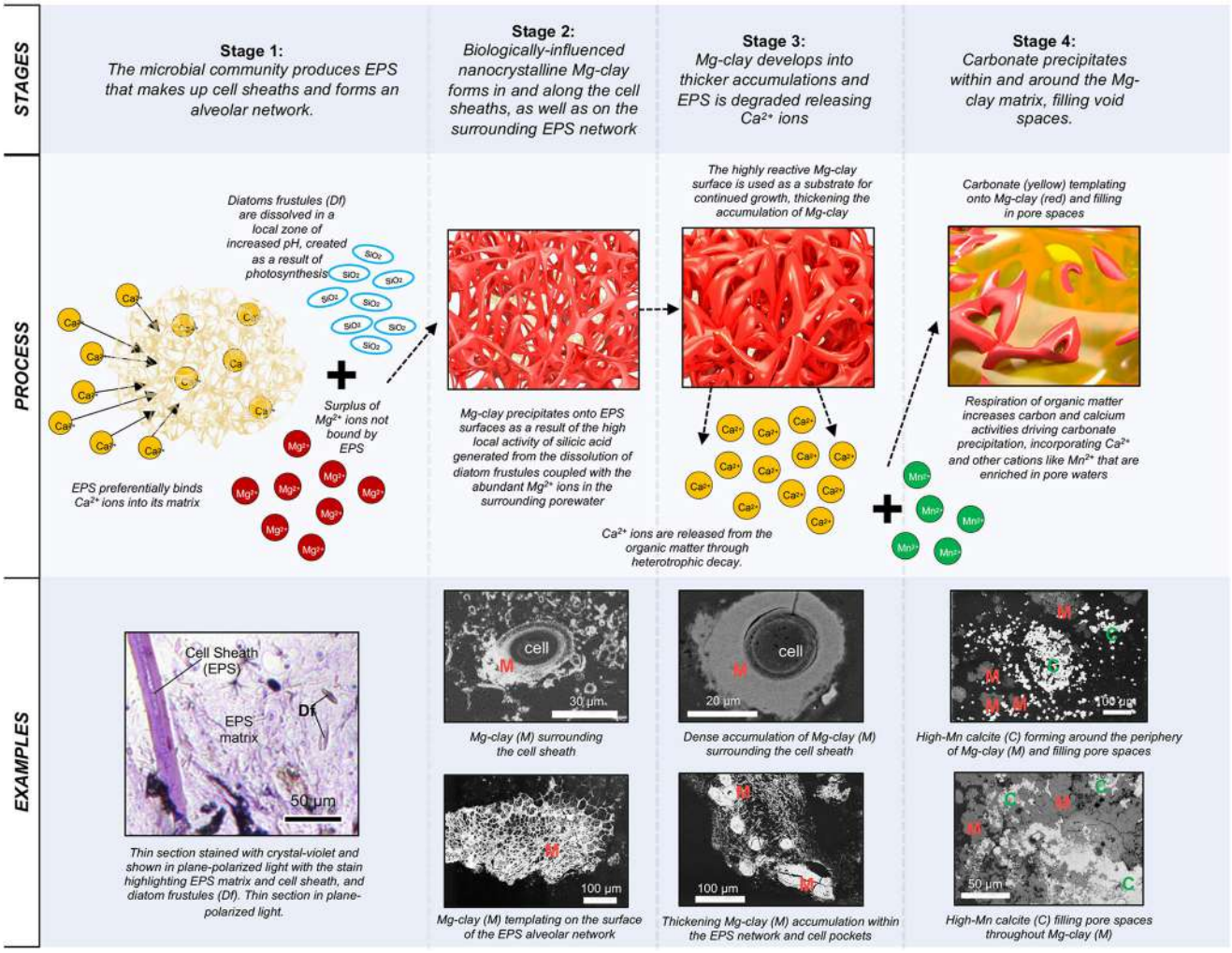

Fig. 8 Summary diagram. Four-stage model showing how Mg-clay pays a critical role in the mineralization pathway for carbonate in the Puquios of the Salar de Llamara.

biologically mediated carbonate in lacustrine environments, and highlight the need to explore additional microbial carbonate depositional environments to determine the presence and influence of Mg-clays.

Conclusions

Observations from this study indicate that Mg-clay plays a critical role in carbonate precipitation through the following mineralization pathway:

1. The microbial community produces EPS that constitutes cell sheaths and forms an alveolar network; the EPS preferentially binds Ca^{2+} ions into its matrix.
2. Biologically-influenced nanocrystalline Mg-clay forms in and along the cell sheaths, as well as on the surrounding EPS network as a result of the high local activity of silicic acid generated from the dissolution of diatom frustules, coupled with abundant Mg^{2+} ions in the surrounding porewater.
3. Mg-clay develops into thicker accumulations, while EPS degrades and releases Ca^{2+} ions.
4. Carbonates precipitate within and around the Mg-clay matrix and fill void spaces; degradation of organic matter increases carbon and calcium activities driving carbonate precipitation, incorporating Ca^{2+} and other cations like Mn^{2+} that are enriched in pore waters.

Mg-clay was identified as precursor to the precipitation of carbonate minerals in the Salar de Llamara. Due to the high reactivity of the clay, brine chemistry in its immediate microenvironment is modified, helping to overcome kinetic barriers for carbonate precipitation. Additionally, clay surfaces serve as ideal substrates for the nucleation of carbonate minerals. As this association between Mg-clays and carbonate minerals is increasingly being recognized across a wide range of depositional environments in both modern and ancient settings, often in association with microbialites, we suggest that carbonate precipitation via a clay precursor may be a common precipitation pathway. These findings result in a shift in our understanding of how microbes influence mineralization pathways and highlight the need to explore additional microbial carbonate depositional environments for the presence and influence of Mg-clays.

Materials and methods

Field studies, sample collection, and environmental data. The samples used in this study were collected during two different field seasons. An orange/brown bulbous mat sample was collected from pond P163 in November 2017, and an orange gel mat sample was collected from pond P31 in March 2019 (Fig. 1). Both samples were preserved in formalin. Environmental parameters of pond water were measured at the time of sample collection using a Hanna 9289 Multiparameter Meter (resolution and accuracy listed in Supplemental Table S2), including pH, oxidation-reduction potential (ORP), electrical conductivity (EC), salinity,

Table 2 FIB-SEM nanotomography parameters for volumetric reconstruction of data.

Sample	Sample Location	Pixel size	Image size (px)	Image size (µm)	Image acquisition interval	Number of images	Reconstructed volume ($µm^3$)
P105	P163	5.4 nm	3072 × 2048	16.57 × 11.05	30 nm	463	13.89
P31A	P31	6.2 nm	3072 × 2048	19.93 × 13.29	25 nm	376	9.4
P31B	P31	3 nm	3072 × 2048	9.23 × 6.16	25 nm	371	9.275

dissolved oxygen (DO), and turbidity. The measurements were made with the probe resting on the bottom substrate of the pond.

Sample preparation. Samples were embedded in epoxy following the method of Nye et al.[66], which preserves both biological and mineral material, in an effort to examine microbe-mineral interactions. After samples were fully cured, the epoxy block from P163 was subsampled and used to prepare petrographic thin sections for optical microscopy examination, and also stained with crystal violet to highlight biomass. The remaining epoxy block from P163, as well as the epoxied sample from P31, were then polished in graduated steps up to 0.6 µm with diamond polishing compound to achieve a flat surface for examination using a scanning electron microscope (SEM). Regions of interest (ROIs) were selected for focused ion beam (FIB)-SEM nanotomography to reconstruct the 3D nanocrystal morphology of the Mg-clay minerals, their location around preserved cell sheaths, as well as the juxtaposition between Mg-clay and carbonate minerals. The surfaces of the SEM samples were coated with a ~15-nm-thick veneer of carbon. Transmission electron microscope (TEM) imaging and selected-area electron diffraction (SAED), and three-dimensional electron diffraction [3DED][67], were used for mineral identification.

Microscopy

Optical microscopy. Thin sections were examined using a Nikon Optiphot series microscope in plane-polarized and cross-polarized light at the Smithsonian National Museum of Natural History, Department of Mineral Sciences.

SEM. SEM imaging was performed at the Smithsonian National Museum of Natural History using a ThermoFisher Scientific Apreo Field Emission SEM. Images were captured in angular backscatter mode at an acceleration voltage of 15 kV, with a working distance of ~10 mm. Elemental composition of mineral phases was determined using an EDAX Octane Energy Dispersive X-Ray Spectrometer (EDS).

FIB-SEM nanotomography. FIB-SEM nanotomography was performed at the George Washington University Nanofabrication and Imaging Center using a Helios NanoLab 660 dual beam focused ion beam SEM, and was conducted in three areas. In sample P163 we targeted an area with Mg-clay nanocrystals in the initial stages of formation around a cyanobacterial cell. In sample P31, we milled an area containing a dense aggregation of Mg-clay along a filamentous cell (P31a), and an area containing both Mg-clay and carbonate (P31b). The ROIs were prepared using ion beam induced deposition to lay down a 1 µm-thick platinum pad to protect the sample from FIB damage. Trenches were milled out on three sides of the ROI, with a large front trench to allow imaging of the cleaned cross-section and two side trenches to minimize the re-deposition effects associated with the milling process. Fiducial markers were created on the sample surface and on the backwall of one of the side trenches to assist with FIB and electron beam alignment, respectively. FIB milling was done using an acceleration voltage of 30 kV and beam current 2.5–21 nA, at 52° stage tilt, and 4 mm working distance. Backscattered electron imaging was performed with the Through the Lens Detector in immersion mode, with an acceleration voltage of 2 kV and beam current 0.4 nA, at 45°stage tilt and working distance of 2.5 mm. The image acquisition parameters for the three datasets are listed in Table 2. The resulting images were aligned using the open-source platform Fiji[68]. The aligned image stacks were imported in the Object Research Systems Dragonfly software package, which was used to segment the stacks in order to define the mineral components, and subsequently reconstruct the ROIs.

TEM. A lamella (<100 nm thickness) from P31 was prepared at George Washington University Nanofabrication and Imaging Center using a Helios NanoLab 660 dual beam focused ion beam SEM equipped with ThermoFisher Scientific EasyLift nanomanipulator for TEM sample lift-out. The lamella was analyzed by TEM using the methods in Heaney et al.[69]. TEM imaging, SAED, and 3DED were performed at the Center for Nanotechnology Innovation, Istituto Italiano di Tecnologia, with a Zeiss Libra 120 TEM operating at 120 kV and equipped with a LaB6 source and a Bruker EDX XFlash6T-60 detector. A camera length of 180 mm was used for both SAED and 3DED experiments, equivalent to a resolution in reciprocal space up to 0.8 Å. Diffraction data were recorded by an ASI Timepix single-electron camera[70]. SAED patterns were analyzed using ImageJ. For the 3DED experiments, multiple data collections were performed in angular steps of 1° with total tilt ranges up to 80°. After each tilt, a diffraction pattern was acquired, and the crystal position tracked. During the experiment, the beam was precessed around the optical axis by an angle of 1°[71]. 3DED data analysis, including 3D reconstruction, diffraction space visualization, and cell parameter determination was performed using the software ADT3D[72].

Data availability

The dataset presented in this study to generate the supplemental videos are available at https://doi.org/10.17632/fw63t9h56p.1 The corresponding author welcomes email contact from the community regarding questions about datasets and products.

Received: 1 April 2022; Accepted: 13 December 2022;
Published online: 24 December 2022

References

1. Burne, R. V. et al. Stevensite in the modern thrombolites of Lake Clifton, Western Australia: A missing link in microbialite mineralization? *Geology* **42**, 575–578 (2014).
2. Zeyen, N. et al. Formation of low-T hydrated silicates in modern microbialites from Mexico and implications for microbial fossilization. *Front. Earth Sci.* **3**, 1–23 (2015).
3. Pace, A. et al. Microbial and diagenetic steps leading to the mineralisation of Great Salt Lake microbialites. *Sci. Rep.* **6**, 1–12 (2016).
4. Wacey, D., Urosevic, L., Saunders, M. & George, A. D. Mineralisation of filamentous cyanobacteria in Lake Thetis stromatolites, Western Australia. *Geobiology* **16**, 203–215 (2018).
5. Chong Díaz, G. Die Salare in Nordchile - Geologie, Struktur und Geochemie. *Geotektonische Forschungen* (1984). Schweizerbart'sche Verlagsbuchhandlung, Stuttgart ©1984.
6. Chong Diaz, G., Demergasso, C., Urrutia Meza, J., Vargas A., M. El Dominio Salino del norte de Chile y sus yacimientos de minerales industriales. *Boletín de la Sociedad Geológica Mexicana* **72**, 1–59 (2020).
7. Otálora, F. et al. Hydrochemical and Mineralogical Evolution through Evaporitic Processes in Salar de Llamara Brines (Atacama, Chile). *ACS Earth Sp. Chem.* **4**, 882–896 (2020).
8. Pueyo, J. J., Chong, G. & Jensen, A. Neogene evaporites in desert volcanic environments: Atacama Desert, northern Chile. *Sedimentology* **48**, 1411–1431 (2001).
9. Ritter, B., Binnie, S. A., Stuart, F. M., Wennrich, V. & Dunai, T. J. Evidence for multiple Plio-Pleistocene lake episodes in the hyperarid Atacama Desert. *Quat. Geochronol.* **44**, 1–12 (2018).
10. López, P. L., Auqué, L. F., Garcés, I. & Chong, G. Características geoquímicas y pautas de evolución de las salmueras superficiales del Salar de Llamara, Chile. *Revista geológica de Chile* **26**, 89–108 (1999).
11. Garcés, I. et al. Características geoquímicas generales del sistema salino del Salar de Llamara (Chile). *Estud. Geológicos* **52**, 23–35 (1996).
12. Reid, R. P. et al. Electrical conductivity as a driver of biological and geological spatial heterogeneity in the Puquios, Salar de Llamara, Atacama Desert, Chile. *Sci. Rep.* **11**, 1–18 (2021).
13. Suosaari, E. P. et al. Environmental and biological controls on sedimentary bottom types. *Geosci.* (2022).
14. Oehlert, A. M. et al. Physical, chemical, and microbial feedbacks controlling brine geochemistry and lake morphology in polyextreme salar environments. *Sci. Total Environ.* **836**, 19 (2022).
15. Eugster, H. P. & Hardie, L. A. Saline Lakes BT - Lakes: Chemistry, Geology, Physics. In (ed. Lerman, A.) 237–293 (Springer New York, 1978). https://doi.org/10.1007/978-1-4757-1152-3_8.
16. Eugster, H. P. Geochemistry of Evaporitic Lacustrine Deposits. *Annu. Rev. Earth Planet. Sci.* **8**, 35–63 (1980).
17. Decho, A. W. Microbial biofilms in intertidal systems: an overview. *Cont. Shelf Res.* **20**, 1257–1273 (2000).
18. Badaut, D. & Risacher, F. Authigenic smectite on diatom frustules in Bolivian saline lakes. *Geochim. Cosmochim. Acta.* **47**, 363–375 (1983).

19. Tosca, N. J. & Masterson, A. L. Chemical controls on incipient Mg-silicate crystallization at 25 °C: Implications for early and late diagenesis. *Clay Miner.* **49**, 165–194 (2014).
20. Tosca, N. J. & Wright, V. P. The Formation and Diagenesis of Mg-Clay Minerals in Lacustrine Carbonate Reservoirs. in *Adapted from oral presentation given at 2014 AAPG Annual Convention and Exhibition* (2014).
21. Decho, A. W. Overview of biopolymer-induced mineralization: What goes on in biofilms? *Ecol. Eng.* **36**, 137–144 (2010).
22. Braissant, O. et al. Characteristics and turnover of exopolymeric substances in a hypersaline microbial mat. *FEMS Microbiol. Ecol.* **67**, 293–307 (2009).
23. Iler, R. K. *The Chemistry of Silicaa: Solubility, Polymerization, Colloid and Surface Properties and Biochemistry of Silica*. (Wiley-Interscience, 1979).
24. Chin, W.-C., Orellana, M. V. & Verdugo, P. Spontaneous assembly of marine dissolved organic matter into polymer gels. *Nature* **391**, 568–572 (1998).
25. Pace, A. et al. Formation of stromatolite lamina at the interface of oxygenic–anoxygenic photosynthesis. *Geobiology* **16**, 378–398 (2018).
26. Arp, G., Thiel, V., Reimer, A., Michaelis, W. & Reitner, J. Biofilm exopolymers control microbialite formation at thermal springs discharging into the alkaline Pyramid Lake, Nevada, USA. *Sediment. Geol.* **126**, 159–176 (1999).
27. Arp, G. et al. Photosynthesis versus Exopolymer Degradation in the Formation of Microbialites on the Atoll of Kiritimati, Republic of Kiribati, Central Pacific. *Geomicrobiol. J.* **29**, 29–65 (2012).
28. Dupraz, C. & Visscher, P. T. Microbial lithification in marine stromatolites and hypersaline mats. *Trends Microbiol.* **13**, 429–438 (2005).
29. Pacton, M., Fiet, N. & Gorin, G. E. Bacterial activity and preservation of sedimentary organic matter: The role of exopolymeric substances. *Geomicrobiol. J.* **24**, 571–581 (2007).
30. Obst, M., Wehrli, B. & Dittrich, M. CaCO3 nucleation by cyanobacteria: laboratory evidence for a passive, surface-induced mechanism. *Geobiology* **7**, 324–347 (2009).
31. Spitzer, S. et al. Effect of Variable pCO2 on Ca2+ Removal and Potential Calcification of Cyanobacterial Biofilms —An Experimental Microsensor Study. *Geomicrobiol. J.* **32**, 304–315 (2015).
32. Barker, P. Differential diatom dissolution in Late Quaternary sediments from Lake Manyara, Tanzania: an experimental approach. *J. Paleolimnol.* **7,** 235–251 (1992).
33. Ryves, D. B. Diatom dissolution in saline lake sediments. An experimental study in the Great Plains of North America. (University College London, 1994).
34. Kaźmierczak, J. et al. Caco3 precipitation in multilayered cyanobacterial mats: Clues to explain the alternation of micrite and sparite layers in calcareous stromatolites. *Life* **5**, 744–769 (2015).
35. Kremer, B., Kaźmierczak, J. & Kempe, S. Authigenic replacement of cyanobacterially precipitated calcium carbonate by aluminium-silicates in giant microbialites of Lake Van (Turkey). *Sedimentology* **66**, 285–304 (2019).
36. Dupraz, C. et al. Processes of carbonate precipitation in modern microbial mats. *Earth-Science Rev.* **96**, 141–162 (2009).
37. Xu, J. et al. Testing the cation-hydration effect on the crystallization of Ca–Mg–CO3 systems. *Proc. Natl. Acad. Sci.* **110**, 17750–17755 (2013).
38. Sun, W., Jayaraman, S., Chen, W., Persson, K. A. & Ceder, G. Nucleation of metastable aragonite CaCO3 in seawater. *Proc. Natl. Acad. Sci.* **112**, 3199–3204 (2015).
39. Molnár, Z., Pekker, P., Dódony, I. & Pósfai, M. Clay minerals affect calcium (magnesium) carbonate precipitation and aging. *Earth Planet. Sci. Lett.* **567**, 116971 (2021).
40. Défarge, C., Trichet, J., Maurin, A. & Hucher, M. Kopara in Polynesian atolls: early stages of formation of calcareous stromatolites. *Sediment. Geol.* **89**, 9–23 (1994).
41. Dupraz, C., Visscher, P. T., Baumgartner, L. K. & Reid, R. P. Microbe-mineral interactions: Early carbonate precipitation in a hypersaline lake (Eleuthera Island, Bahamas). *Sedimentology* **51**, 745–765 (2004).
42. López-García, P. et al. Bacterial diversity and carbonate precipitation in the giant microbialites from the highly alkaline Lake Van, Turkey. *Extremophiles* **9**, 263–274 (2005).
43. Berner, R. A. The role of magnesium in the crystal growth of calcite and aragonite from sea water. *Geochim. Cosmochim. Acta.* **39**, 489–504 (1975).
44. Altermann, W., Kazmierczak, J., Oren, A. & Wright, D. T. Cyanobacterial calcification and its rock-building potential during 3.5 billion years of Earth history. *Geobiology* **4**, 147–166 (2006).
45. Burne, R. V. The Role and Significance of Authigenic Magnesium Silicates in the Organomineralisation of Microbialites in the Yalgorup Lakes, Western Australia. *Masters Thesis Australian National University* (The Australian National University, 2016).
46. Souza-Egipsy, V., Wierzchos, J., Ascaso, C. & Nealson, K. H. Mg-silica precipitation in fossilization mechanisms of sand tufa endolithic microbial community, Mono Lake (California). *Chem. Geol.* **217**, 77–87 (2005).
47. Arp, G., Reimer, A. & Reitner, J. Microbialite Formation in Seawater of Increased Alkalinity, Satonda Crater Lake, Indonesia. *J. Sediment. Res.* **73**, 105–127 (2003).
48. Des Marais, D. J. et al. The NASA Astrobiology Roadmap. *Astrobiology* **8**, 715–730 (2008).
49. Hays, L. E. et al. Biosignature Preservation and Detection in Mars Analog Environments. *Astrobiology* **17**, 363–400 (2017).
50. Chan, M. A. et al. Deciphering Biosignatures in Planetary Contexts. *Astrobiology* **19**, 1075–1102 (2019).
51. Potter-McIntyre, S. L., Williams, J., Phillips-Lander, C. & O'Connell, L. Taphonomy of Microbial Biosignatures in Spring Deposits: A Comparison of Modern, Quaternary, and Jurassic Examples. *Astrobiology* **17**, 216–230 (2017).
52. Nyirő-Kósa, I. et al. Nucleation and growth of Mg-bearing calcite in a shallow, calcareous lake. *Earth Planet. Sci. Lett.* **496**, 20–28 (2018).
53. Léveillé, R. J., Fyfe, W. S. & Longstaffe, F. J. Geomicrobiology of carbonate-silicate microbialites from Hawaiian basaltic sea caves. *Chem. Geol.* **169**, 339–355 (2000).
54. Bontognali, T. R. R. et al. Dolomite formation within microbial mats in the coastal sabkha of Abu Dhabi (United Arab Emirates). *Sedimentology* **57**, 824–844 (2010).
55. Banfield, J. F., Jones, B. F. & Veblen, D. R. An AEM-TEM study of weathering and diagenesis, Abert Lake, Oregon: II. Diagenetic modification of the sedimentary assemblage. *Geochim. Cosmochim. Acta.* **55**, 2795–2810 (1991).
56. Hay, R. L. et al. Clay Mineral Diagenesis in Core KM-3 of Searles Lake, California. *Clays Clay Miner.* **39**, 84–96 (1991).
57. Hover, V. C., Walter, L. M., Peacor, D. R. & Martini, A. M. Mg-smectite authigenesis in a marine evaporative environment, Salina Ometepec, Baja California. *Clays Clay Miner.* **47**, 252–268 (1999).
58. Gérard, E. et al. Key role of Alphaproteobacteria and Cyanobacteria in the formation of stromatolites of Lake Dziani Dzaha (Mayotte, Western Indian Ocean). *Front. Microbiol.* **9**, 1–20 (2018).
59. Bristow, T. F. et al. Mineralogical constraints on the paleoenvironments of the Ediacaran Doushantuo Formation. *Proc. Natl. Acad. Sci.***106**, 13190–13195 (2009).
60. Zeyen, N. et al. Geochemical Conditions Allowing the Formation of Modern Lacustrine Microbialites. *Procedia Earth Planet. Sci.* **17**, 380–383 (2017).
61. Zeyen, N. et al. Integrative analysis of the mineralogical and chemical composition of modern microbialites from ten Mexican lakes: What do we learn about their formation? *Geochim. Cosmochim. Acta.* **305**, 148–184 (2021).
62. Setti, M., Marinoni, L. & López-Galindo, A. Mineralogical and geochemical characteristics (major, minor, trace elements and REE) of detrital and authigenic clay minerals in a Cenozoic sequence from Ross Sea, Antarctica. *Clay Miner.* **39**, 405–421 (2004).
63. Huang, J., Chu, X., Lyons, T. W., Planavsky, N. J. & Wen, H. A new look at saponite formation and its implications for early animal records in the Ediacaran of South China. *Geobiology* **11**, 3–14 (2013).
64. Konhauser, K. O. & Urrutia, M. M. Bacterial clay authigenesis: a common biogeochemical process. *Chem. Geol.* **161**, 399–413 (1999).
65. Awramik, S. M. & Buchheim, H. P. Giant Microbialites from the Green River Formation, Laney Member, Sand Wash Basin, Colorado. **50984**, 1–5 (2014).
66. Nye, O. B., Dean, D. A. & Hinds, R. W. Improved Thin Section Techniques for Fossil and Recent Organisms Published by: SEPM Society for Sedimentary Geology Stable URL: https://www.jstor.org/stable/1302848 REFERENCES Linked references are available on JSTOR for this article: **46**, 271–275 (1972).
67. Gemmi, M. et al. 3D electron diffraction: The nanocrystallography revolution. *ACS Cent. Sci.* **5**, 1315–1329 (2019).
68. Schindelin, J. et al. Fiji: an open-source platform for biological-image analysis. *Nat. Methods.* **9**, 676–682 (2012).
69. Heaney, P. J., Vicenzi, E. P., Giannuzzi, L. A. & Livi, K. J. T. Focused Ion Beam (Fib) Preparation of Tem. *Am. Mineral.* **86**, 1094–1099 (2001).
70. Nederlof, I., van Genderen, E., Li, Y.-W. & Abrahams, J. P. A Medipix quantum area detector allows rotation electron diffraction data collection from submicrometre three-dimensional protein crystals. *Acta Crystallogr. Sect. D.* **69**, 1223–1230 (2013).
71. Mugnaioli, E., Gorelik, T. & Kolb, U. "Ab initio" structure solution from electron diffraction data obtained by a combination of automated diffraction tomography and precession technique. *Ultramicroscopy* **109**, 758–765 (2009).
72. Kolb, U., Mugnaioli, E. & Gorelik, T. E. Automated electron diffraction tomography – a new tool for nano crystal structure analysis. *Cryst. Res. Technol.* **46**, 542–554 (2011).

Acknowledgements

We thank the SQM Ltd., FisioAqua, and S. Swaminathan for logistical and field support; T. Gooding, S. Whittaker, and J. Wingerath for technical assistance with sample preparation and SEM analyses. I.L. is grateful for a Smithsonian Institution Edward and Helen Hintz Secretarial Scholarship. Samples were obtained with permission from SQM Ltd.

Author contributions

E.P.S., I.L., and R.P.R. wrote the main manuscript text. Samples were collected by E.P.S., R.P.R., A.M.O., and A.T.P. Samples were prepared by E.P.S. and P.F.M. Electron microscopy was completed by E.P.S. and P.F.M. FIB-SEM was completed by P.P., I.L., and E.P.S. 3D reconstructions were completed by I.L. TEM and SAED analyses were completed by E. M. and M.G. E.P.S., I.L., A.M.O., P.P., E.M., M.G., P.F.M., A.M.P., and R.P.R. reviewed and edited the manuscript.

Competing interests

The authors declare no competing interests.

Additional information

Supplementary information The online version contains supplementary material available at https://doi.org/10.1038/s43247-022-00658-5.

Correspondence and requests for materials should be addressed to Erica P. Suosaari.

Peer review information Communications Earth & Environment thanks Michael C. Pope and the other, anonymous, reviewer(s) for their contribution to the peer review of this work. Primary Handling Editors: Mojtaba Fakhraee, Joe Aslin.

Reprints and permission information is available at http://www.nature.com/reprints

Publisher's note Springer Nature remains neutral with regard to jurisdictional claims in published maps and institutional affiliations.

Open Access This article is licensed under a Creative Commons Attribution 4.0 International License, which permits use, sharing, adaptation, distribution and reproduction in any medium or format, as long as you give appropriate credit to the original author(s) and the source, provide a link to the Creative Commons license, and indicate if changes were made. The images or other third party material in this article are included in the article's Creative Commons license, unless indicated otherwise in a credit line to the material. If material is not included in the article's Creative Commons license and your intended use is not permitted by statutory regulation or exceeds the permitted use, you will need to obtain permission directly from the copyright holder. To view a copy of this license, visit http://creativecommons.org/licenses/by/4.0/.

© The Author(s) 2022